Journal of Materials Chemistry

Cite this: J. Mater. Chem., 2012, 22, 21533

www.rsc.org/materials

PAPER

One-step vapor–solid reaction growth of Sn@C core–shell nanowires as an anode material for Li-ion batteries†

Kai-Chieh Hsu,[a] Chia-Erh Liu,[a] Po-Chin Chen,[b] Chi-Young Lee[b] and Hsin-Tien Chiu*[a]

Received 16th July 2012, Accepted 28th August 2012
DOI: 10.1039/c2jm34654k

Sn@C core–shell nanowires (NWs) were synthesized by reacting SnO_2 particles with a flowing mixture of C_2H_2 and Ar gases at elevated temperatures. The overall diameter of the core–shell nanostructure was 100–350 nm. The C shell thickness was 30–70 nm. The NW length was several micrometers. Inside the shell, a void space was found. The reaction is proposed to be *via* a vapor–solid reaction growth (VSRG) pathway. The NWs were investigated as a potential anode material for Li-ion batteries (LIBs). The half-cell constructed from the as-fabricated electrode and a Li foil exhibited a reversible capacity of 525 mA h g^{-1} after one hundred cycles at a current density of 100 mA g^{-1}. At a current density as high as 1000 mA g^{-1}, the battery still maintained a capacity of 486 mA h g^{-1}. The excellent performance is attributed to the unique 1D core–shell morphology. The core–shell structure and the void space inside the shell can accommodate large volume changes caused by the formation and decomposition of Li_xSn alloys in the charge–discharge steps.

1. Introduction

Rechargeable lithium-ion batteries (LIBs) are important energy storage devices for mobile electronics, electric vehicles and renewable energy systems.[1,2] To meet these applications, LIBs with high specific storage capacity and good cycle properties are essential.[3] Many research results related to improving the performance and cycle life of high-capacity electrode materials, such as Fe_3O_4, MgH_2, Si, Si/C, Sn, and Sn-based composites, in LIBs have been published.[4–15] Among them, metallic Sn has been demonstrated as a potential anode material for LIBs because of its high lithium-ion storage capacity.[9–11] Its theoretical specific capacity ($Li_{4.4}Sn$, 992 mA h g^{-1}) is much higher than that of graphitic carbon (LiC_6, 372 mA h g^{-1}).[16–18] However, significant capacity fading after cycling has been a serious problem for Sn containing electrode materials. This has been attributed to enormous volume changes during charging and discharging processes leading to particle fracture and aggregation.[19] In some cases, the volume expansion after cycling steps can be as high as 259%.[17,19] In order to solve the volume expansion and fracture problems, a couple of new strategies have been explored recently. In one strategy, various Sn-containing composite materials, including core–shell structures and nanocomposites, are employed to improve the capacity and the electrochemical performance.[9–11,14,21–26] For example, nanostructured Sn encapsulated in a hollow carbon shell can improve the electrode performance.[26] The shell acts as a barrier to prevent aggregation of Sn and provides a void space for the volume changes.[22] Nanoparticles of Sn embedded in a C-based matrix also perform well.[14] Other representative cases are summarized in Table S1 in the ESI.† In the other strategy, mesoporous Sn is used as the anode to demonstrate improved performance.[15]

Previously, we developed a vapor–solid reaction growth (VSRG) strategy to fabricate one-dimensional (1D) heterostructures. These include cable-like Cu nanowires (NWs), *a*-silica encapsulated Ag NWs, CaF_2@*a*-C core–shell NWs, and tubular SiC.[27–30] In the reactions, a vapor phase reactant was reacted with a solid. The as-grown solid products underwent phase-segregation and developed into 1D core–shell nanostructures. By using this strategy, we have designed a reaction in this study by employing vapor phase C_2H_2 and SnO_2 solid particles as the reactants to grow Sn@C core–shell NWs. The NWs are shown to be a stable electrode material, which leads to excellent electrochemical performance in coulombic efficiency, rate capability and capacity retention. Our observations are presented below.

2. Experiment

2.1 Growth of Sn@C core–shell NWs

The growths were carried out inside a hot-wall reactor composed of a Lindberg tubular furnace and a quartz tube (diameter 27 mm). A summary of the experimental conditions for the preparation of A and B is given in Table 1. SnO_2 powders (0.20 g, 1.3 mmol, Sigma-Aldrich) were uniformly placed in a quartz

[a]*Department of Applied Chemistry, National Chiao Tung University, Hsinchu, Taiwan, 30050, R. O. C. E-mail: htchiu@faculty.nctu.edu.tw*
[b]*Department of Materials Science and Engineering, National Tsing Hua University, Hsinchu, Taiwan, 30043, R. O. C.*

† Electronic supplementary information (ESI) available: Additional tables of literature summaries, SEM and TEM images, EDX and XRD patterns, Raman spectra and TGA data. See DOI: 10.1039/c2jm34654k

Table 1 Summary of Sn@C NW samples

Sample	SnO_2 size (μm)	C_2H_2 (sccm)	Ar (sccm)	Growth temperature (K)	Growth time (h)	Morphology	Sn–C at% ratio	Electrochemical performance
A	0.1	3	150	973	8	Length 2–5 μm, diameter 200–350 nm, shell thickness 30–70 nm	8.1/91.9	525 mA h g^{-1} at 100 mA g^{-1} [b] 486 mA h g^{-1} at 1000 mA g^{-1} [b] 290 mA h g^{-1} at 3000 mA g^{-1} [b]
B[a]	5	3	90	923	10	Length 5–10 μm, diameter 150–200 nm, shell thickness 30–70 nm	11.0/89.0	102 mA h g^{-1} at 100 mA g^{-1} [c]

[a] Contained unreacted SnO_2 24.5%. Estimated from the relative intensity ratio of SnO_2 (110)/Sn (200) (0.68/0.32) in the XRD pattern. [b] 0.005–2 V, after 100 cycles. [c] 0.005–3 V, after 50 cycles.

boat (length 10 cm) at the center of the furnace. At atmospheric pressure, C_2H_2 (3 sccm) mixed with Ar was passed into the reactor and reacted with SnO_2 at a designated temperature and time period. After the reactor was cooled naturally in Ar to room temperature, black products were collected.

2.2 Materials characterizations

Samples were characterized by XRD using a Bruker AXS D8 Advance with Cu $K_{\alpha 1}$ radiation. SEM images and EDX spectra were taken with a Hitachi S-4000, a Hitachi S-4700I and a JEOL JSM-7401F operated at 15 keV. TEM, ED, HRTEM images and EDX data were acquired on a JEOL JEM-3000F at 300 kV and a JEOL JEM-2010 at 200 kV. Raman spectra were measured by a high resolution confocal Raman microscope (Horiba, LabRAM HR800) with an excitation wavelength of 633 nm and a portable Raman spectrometer (MiniRam II Raman spectrometer system) with an excitation wavelength of 785 nm. TGA studies were conducted using a Netzsch STA 409 PC in an O_2 environment to estimate Sn and C contents in samples.

2.3 Electrochemical tests

Electrochemical measurements were performed with a battery test system (Arbin Testing System). Typically, a two-electrode 2032 coin-type cell employing one of the composite powders and a Li foil as the electrodes was assembled in a dry room. An *N*-methyl pyrrolidone (NMP) slurry, prepared by mixing the composite powder, carbon black (Super-P), and the binder poly-(vinylidene fluoride) (PVDF) with a weight ratio of 80 : 10 : 10 was uniformly applied on to a Cu foil (thickness 14 μm). The foil was vacuum dried (403 K) overnight, compressed, cut into disks (diameter 14 mm), and combined with the electrolyte and the other electrode. The electrolyte was made of $LiClO_4$ dissolved in a mixture of ethylene carbonate (EC) and dimethyl carbonate (DMC) (1.0 M, volume ratio 1 : 1). A Li plate was cut into disks (diameter, 14 mm) and used as both the reference and the counter electrode. CV experiments were carried out using a CHI 6081C (CH Instruments) electrochemical analyzer. Electrochemical experiments of the coin-type cells were cycled between 0.005 V and 2.0 V at room temperature. During the battery assembly, the amount of the composite was weighed for electrochemical performance estimation. Some of the devices were disassembled after the tests so that the composite solids could be investigated further.

3. Results and discussion

The reactions for the fabrication of Sn@C core–shell NWs were carried out in a horizontal hot-wall quartz tube reactor. SnO_2 powders in a quartz boat inside the reactor were reduced at high temperatures by a flowing mixture of C_2H_2 and Ar at atmospheric pressure. At the end of each reaction, black products were collected as the product. By varying the particle sizes and quantity of SnO_2 and the reaction conditions, products with various morphologies were collected. Products A and B, as summarized in Table 1, are listed as the examples in this article.

3.1 Characterization of Sn@C core–shell NWs

Scanning electron microscopic (SEM) images of samples A and B are shown in Fig. 1. In the low magnification views Fig. 1a and c, numerous one-dimensional NWs with lengths up to tens of micrometers are observed. Magnified images in Fig. 1b and d suggest that diameters of the NWs in A and B are hundreds of nanometers. The insets reveal that the NWs contain an apparent core–shell tubular structure. It is easy to perceive the contrast differences displayed within these images, from the side-view and the top-view of the NWs in Fig. 1b and d, respectively. An energy dispersive X-ray (EDX) spectrum of A displayed in Fig. S1 in the ESI† indicates that the core–shell NWs contain both C and Sn. The presence of metallic Sn (JCPDS card file no. 86-2265) in both

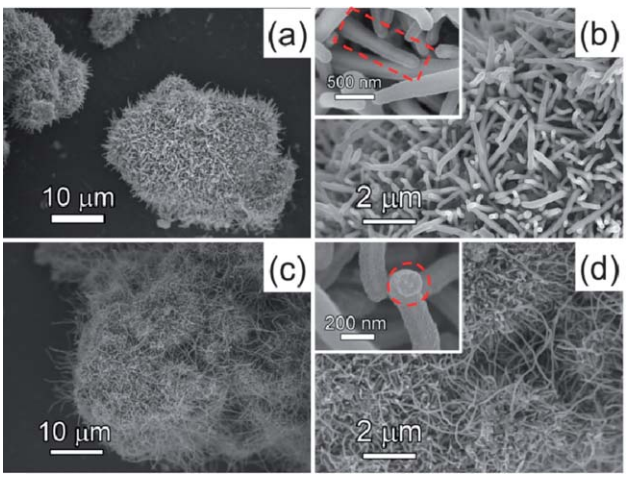

Fig. 1 SEM images. (a) Low and (b) high magnification views of product A. (c) Low and (d) high magnification views of product B. The core–shell structures can be observed in the regions marked in the insets.

A and B is confirmed by the XRD patterns shown in Fig. S2 in the ESI† (ref. 31). Product B, probably due to large original SnO_2 sizes, still contains unreacted SnO_2 as suggested by its diffraction pattern observed in the XRD (JCPDS card file no. 72-1147).[31] In Fig. S3 in the ESI,† Raman spectra of A and unprocessed SnO_2 are compared. For A, two broad bands at 1328 cm^{-1} and 1583 cm^{-1} are observed. They correspond respectively to D band and G band, with a D/G intensity ratio of 1.46, of a less-ordered carbon material.[32–34] Because no signals of SnO_2 are observed, we conclude that A does not contain any unreacted oxide. The quantities of Sn and C in A are estimated using the results from a thermogravimetric analysis (TGA) shown in Fig. S4 in the ESI.† After A was heated to 1273 K in an O_2 environment, obvious weight decrease was observed above 850 K. By assuming all Sn and C in A were fully oxidized, we estimate that the Sn and C contents are 8.1 at% and 91.9 at%, respectively. Morphology of the samples prepared under other reaction conditions is shown in the SEM images in Fig. S5 in the ESI.† From Fig. S5b,† the lowest NW growth temperature is determined to be 923 K.

Results of transmission electron microscopy (TEM) studies of A are shown in Fig. 2. From the images of several samples, Fig. 2a–c, it is confirmed that the NWs have a core–shell structure with diameters 200–350 nm and shell thicknesses 30–70 nm. Inside the shell, in some cases, the inner core fills the space completely, as shown in Fig. 2a. On the other hand, more partially filled NWs are formed, as shown in a couple of examples in Fig. 2b. From a section of a broken NW, low and high magnification views are shown in Fig. 2c and d, respectively. From Fig. 2d, selected area electron diffraction (SAED) patterns are taken and shown in Fig. 2e and f. They correspond to the shell and the core, respectively. Fig. 2e presents a pattern composed of three diffused rings. Starting from the most inside, these are assigned to the reflections from (005), (105) and (202) planes of the less ordered C. A dot pattern displayed in Fig. 2f suggests that the core can be indexed to the 0 0 1 zone axis of single crystalline Sn. From the image, the lattice parameters *a* and *c* of a tetragonal crystal system are estimated to be 0.58 nm and 0.32 nm, respectively.[31] Fig. 2g shows a high resolution lattice image of the core. Two sets of parallel fringes, spaced at 0.29 nm and 0.21 nm, are observed. These are assigned correspondingly to the spacings of {0 2 0} and {2 2 0} planes of crystalline Sn. Combined with the SAED result, the growth of the Sn core is determined to be along the [2 4 0] axis. An EDX spectrum shown in Fig. 2h confirms that the NW contains both C and Sn.

In a series of TEM images presented in Fig. 3, it is suggested that the Sn core inside the C shell was liquefied upon continuous electron beam irradiations, as shown by the extending Sn boundary in the void displayed in the images. The presence of the cavities inside C shells is known to accommodate enormous volume variations during Li alloying and dealloying processes in anodes fabricated from Sn containing materials.[9,10]

3.2 Proposed reaction pathway

Growth of the Sn@C core–shell NWs is further discussed below to illustrate the important features of the reaction. The overall reaction stoichiometry between C_2H_2 and SnO_2 to produce Sn and C could be either

$$2C_2H_2 + SnO_2 \rightarrow Sn + 4C + 2H_2O,$$
$$\Delta G_r^\circ = -372.84 \text{ kJ mol}^{-1}$$

or

$$2C_2H_2 + 2SnO_2 \rightarrow 2Sn + 3C + CO_2 + 2H_2O,$$
$$\Delta G_r^\circ = -247.33 \text{ kJ mol}^{-1}$$

Both reactions are thermodynamically favored due to the negative standard Gibbs free energies of reaction (ΔG_r°).[35] In addition, we suggest that the core–shell NWs are grown *via* a VSRG pathway shown in Scheme 1. It is analogous to the ones

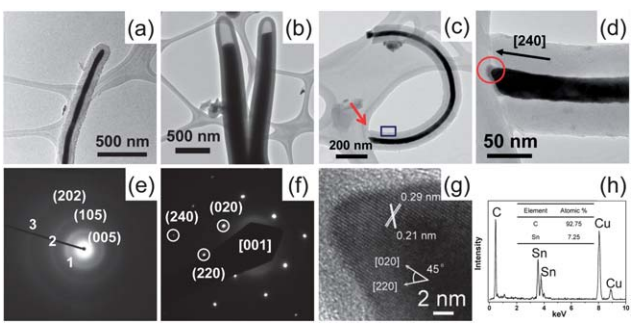

Fig. 2 TEM studies of product A. (a) A completely filled core–shell NW, (b) a pair of partially filled NWs, (c) a section of a broken NW, (d) a high magnification image from the pointed region in (c), (e) SAED pattern from the rectangle area in (c) and (f) SAED pattern from the end of the core in (d). (g) HRTEM image from the region circled in (d). (h) EDX spectrum from (c).

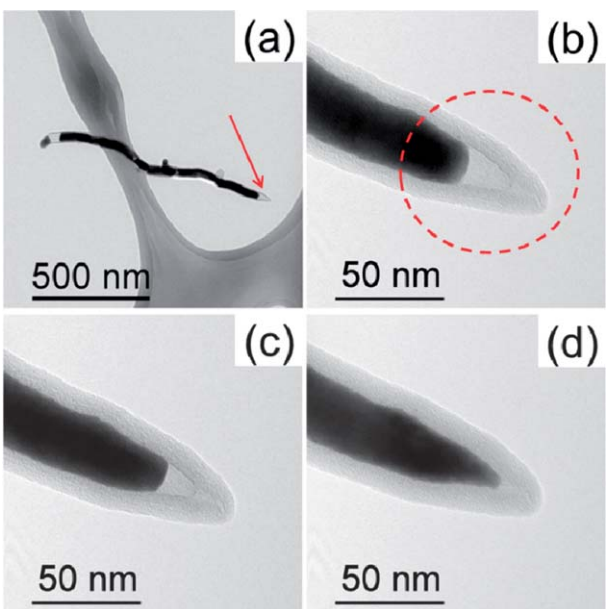

Fig. 3 TEM images of a Sn@C core–shell NW. (a) Low magnification image and (b) high magnification view of the area marked by the arrow in (a) images taken after irradiating the circled area in (b) by an electron beam for (c) 60 s and (d) 180 s. The void shown in the circled area in (b) was filled by melted Sn after the electron beam irradiation.

proposed before for the growths of 1D CaF_2@*a*-C NWs and SiC tubes.[29,30]

The reaction happens at the interface between the vapor phase C_2H_2 and the surface of the SnO_2 solid. From the SEM image displayed in the inset in Fig. S5a in the ESI,† it is discovered that the oxide can be reduced to metallic Sn at 873 K.[36] Due to their large difference in surface energies, the as-formed products are composed of phase-separated Sn and C nanoparticles (NPs). As the Sn NPs coalesce to generate a core, the C NPs covered the Sn surface to form a shell. After more Sn and C products migrate and incorporate into this heterostructured seed, the high melting point C shell solidifies even though the low melting point Sn core stays in the liquid state. Since the solidified C shell possesses a certain width, incorporation of more products into the growing heterostructure can only extend one dimensionally into the observed core–shell NW morphology. In the experiments, growth of small diameter core–shell NWs is observed at 923 K, as shown in Fig. S5b in the ESI.† It is known that as the size of a nanomaterial increases, its melting point increases as well. Thus, we anticipate that the NWs grown at higher temperatures should have larger diameters.

This is supported by the observations shown in Fig. 1b and d and the data summarized in Table 1. The diameters of the NWs in A, grown at 973 K, are wider than those of B, grown at 923 K. The images in Fig. S5b–d in the ESI† also demonstrate that as the growth temperature is increased from 923 K to 1123 K, more and wider NWs are formed. It is worthwhile to mention that the proposed VSRG reaction proceeds *via* steps very different from the ones in typical vapor–liquid–solid (VLS) type growths.[37]

3.3 Electrochemical properties of Sn@C core–shell NWs

According to the literature, employing SnO_2 and Sn for anode applications in LIBs presents several drawbacks. These include the irreversibility associated with the SnO_2 reduction, the capacity losses due to the formation of the solid electrolyte interface (SEI) on the Sn surfaces, and large volume variations during the Li^+ insertion and extraction reaction steps.[38–40] For the Sn@C core–shell NWs prepared in this study, we performed the following electrochemical studies. Half-cells composed of a Li foil, as the negative electrode (anode), and Sn@C core–shell NWs, as the positive electrode (cathode), were assembled into test cells. In Fig. 4a, the first cyclic voltammetric (CV) profile of the NWs shows a reduction peak (cathodic scan) at 1.52 V. The peak is irreversible because it disappears in the later cycles. One possible origin of the peak was from the SEI on Sn.[41] However, another signal peak at 1.05 V usually accompanies the one near 1.52 V. In addition, since most of the Sn containing nanostructures are wrapped inside the C shells, it is less likely that the SEI could form on the Sn surface. The peak at 1.52 V cannot be assigned to the SEI on the C shells either because the reported signals were at 0.80 and 1.25 V.[41] Thus, we ascribe the peak at 1.52 V to the formation of LiOH due to the presence of traces of H_2O in the electrolyte.[42] The other reduction peaks are observed at 0.58 V, 0.46 V and 0.30 V during the discharging/alloying step

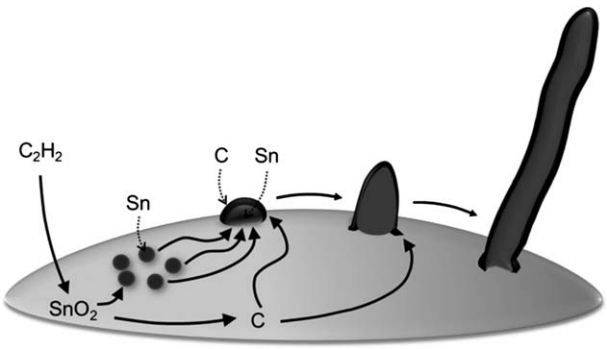

Scheme 1 Proposed VSRG pathway to form Sn@C core–shell NWs.

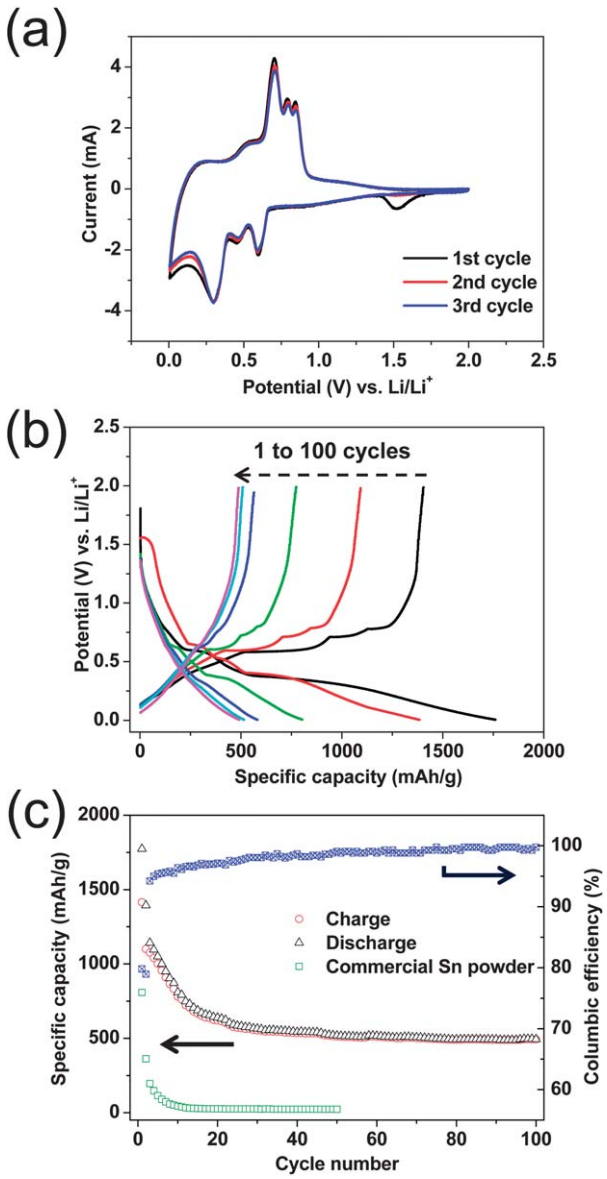

Fig. 4 (a) Cyclic voltammograms of a Sn@C core–shell NW electrode (scan speed 0.5 mV s^{-1}). Electrochemical performance of the electrode cycled between 0.005 V and 2.0 V *vs.* Li/Li^+ (cycling rate 500 mA g^{-1}); (b) voltage profiles of the electrode after 1, 2, 10, 25, 50, and 100 cycles and (c) capacity fading of the electrode. Coulombic efficiency and reversibility of each cycle of the electrode are presented in the secondary *y*-axis on the right of (c). The discharge capacity of an electrode fabricated from commercial Sn powder was cycled at 100 mA g^{-1}.

while the oxidation peaks (anodic scan) are found at 0.54 V, 0.71 V, 0.80 V and 0.85 V during the charging/dealloying step. These are correlated with the interconversions among Sn and several Li_xSn ($0 \leq x \leq 4.4$) phases, including Li_2Sn_5, LiSn, Li_7Sn_3, Li_5Sn_2, $Li_{13}Sn_5$, Li_7Sn_2, and $Li_{4.4}Sn$.[10,17,43,44] Previous studies indicated that primary lithiation and delithiation processes of amorphous carbon and graphite materials usually occurred below 0.25 V while amorphous carbon nanotube (CNT) and single-wall CNT showed Li deintercalation at 0.9–1.2 V.[45–50] The CV profiles in Fig. 4a display gradual current decreases below 0.25 V and no clear deintercalation peaks at 0.9–1.2 V in the initial cycles. The observations suggest that Li^+ ions probably accumulate irreversibly in the carbon shells.

Fig. 4b displays the voltage profiles of the half-cell made of the Sn@C NWs. The data were taken at a cycling rate of 500 mA g^{-1} and between 0.005 and 2.00 V *versus* Li/Li^+. The voltage profiles indicate that the NW electrode exhibits the characteristics of a Sn electrode.[10] The first discharge and charge steps deliver specific capacities of 1760 and 1405 mA h g^{-1}, respectively. They correspond to a coulombic efficiency of 80%. The large initial capacity loss can be attributed, as mentioned above, to the formation of the SEI layer on the electrode surface during the first discharge step and the storage of Li^+ ions in EC/DMC-based electrolytes, which are difficult to be extracted.[10,17,39] The presence of multiple plateaus in the initial discharge–charge curves is assigned to the formation and decomposition of Li_xSn.[43,44] In the following cycles, the plateaus become less and less discernible. For example, the plateaus at 0.58 V (the transition between Sn and LiSn phases) and 0.46 V (the transition between LiSn and Li_7Sn_3 phases) decrease gradually with increasing cycle numbers. These observations agree with the CV results. They suggest that Li^+ ions stored in the related Li_xSn phases may not undergo reversible cycling. The discharge capacities are found to be 1384, 804, 582, 515 and 490 mA h g^{-1} at the second, tenth, twenty-fifth, fiftieth and one hundredth cycles, respectively.

Fig. 4c depicts the specific capacity and the coulombic efficiency of the discharge–charge process of the half-cell with a cycling rate at a current density of 500 mA g^{-1}. Obviously, the capacity dropped swiftly for the first ten cycles. As discussed above, there are several possible pathways which may provide irreversible storage of Li^+ ions. These include the formation of the SEI layer, the decomposition of electrolytes, and the accumulation of Li^+ ions in carbon and tin materials. They offer an apparent capacity which exceeds the theoretical value. Between the twenty-fifth and the fiftieth cycles, the half-cell remains stable during the cycling and exhibits a fade rate of 0.47% per cycle. The half-cell continues to be stable for the next fifty cycles with a fade rate of 0.09% per cycle. The specific capacity is 490 mA h g^{-1} at the end of the one hundredth cycle. The coulombic efficiency remains relatively stable at over 98% after the twenty-fifth cycle. In contrast, the cycling performance of a half-cell constructed from commercial Sn powders (particle size distribution 1–10 μm) at a rate of 100 mA g^{-1} is very poor, as shown in Fig. 4c also.

Fig. 5 shows the cycling rate capability of the half-cell constructed from the Sn@C core–shell NWs with a voltage window of 0.005–2.0 V. Fig. 5a shows the discharge capacities of the device at current densities of 100, 500, 1000, and 3000 mA g^{-1}. After one hundred cycles, the discharge (Li alloying) capacities at these rates are 525, 490, 486, and 286 mA h g^{-1}, respectively.

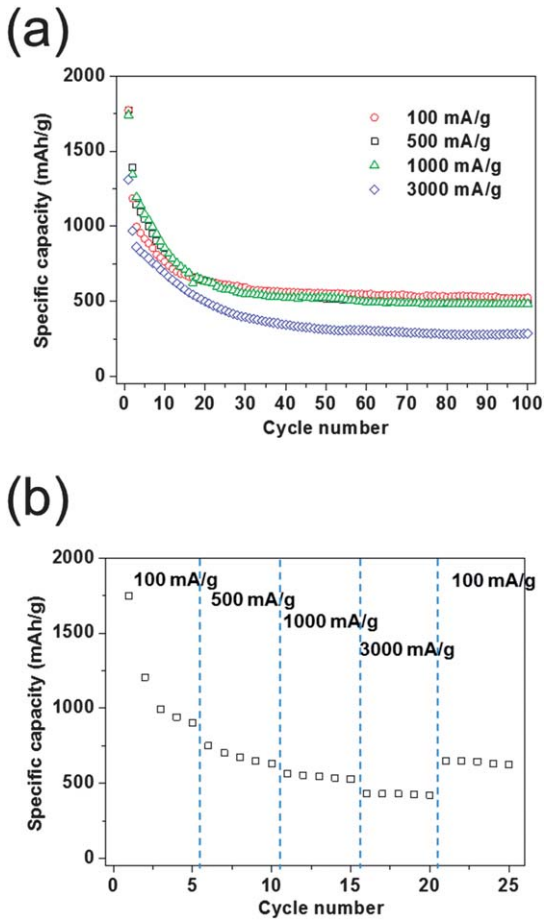

Fig. 5 Electrochemical performance of a Sn@C core–shell NW electrode cycled between 0.005 V and 2.0 V *vs.* Li/Li^+. (a) Curves of specific capacity *versus* cycle number of the electrode at cycling rates of 100 mA g^{-1}, 500 mA g^{-1}, 1000 mA g^{-1} and 3000 mA g^{-1}. (b) Discharge capacities of the electrode as a function of discharge rates (100–3000 mA g^{-1}).

Both of the discharge capacities at 500 and 1000 mA g^{-1}, compared to the one at 100 mA g^{-1}, are about 93%. Even at 3000 mA g^{-1}, 55% of the capacity at 100 mA g^{-1} remained. In Fig. 5b, a capacity of 905 mA h g^{-1} is observed after the battery is cycled at 100 mA g^{-1} for five times. Then, after continued cycling at 500 mA g^{-1}, 1000 mA g^{-1}, and finally 3000 mA g^{-1} for five times each, the half-cell returns back to 626 mA h g^{-1} at 100 mA g^{-1}. This demonstrates that even after fast discharge–charge cycles at 3000 mA g^{-1}, the electrode was not severely degraded and the half-cell still exhibited excellent cycling properties. Consequently, we conclude that the improved electrochemical performance of the half-cell is rooted in the special morphology of the Sn@C core–shell NWs.

The NW structure may shorten the transport lengths for both electrons and Li^+ ions. The C shell layer probably acts as a good electronic conductor and serves as a buffer for the volume change during the lithiation–delithiation process. Fig. S6a and b in the ESI† shows the images of the as-prepared electrode material containing the Sn@C core–shell NWs. After one hundred discharge–charge cycles at 500 mA g^{-1} (cycled between 0.005 and 2.0 V), many Sn@C core–shell NWs still maintain original diameters with clear core–shell structures in Fig. S6c and d in the

ESI.† Clearly, the volume expansion caused by the lithiation of the Sn cores was confined within the C shells. Two possible reasons are proposed to rationalize the observed confinements. One of them is attributed to the voids observed in Fig. 2 and 3, which may accommodate some of the expansions. The other one may originate from the flexible amorphous C shells which could be deformed extensively during the volume variations.[51] In Fig. S6c and d,† only some NWs are found to be destructed into aggregated particles, probably due to non-uniform volume changes. On the other hand, as shown in Fig. S7 in the ESI,† the electrode fabricated from commercial Sn powders shows severe aggregations after fifty discharge–charge cycles. Because the NWs retain most of the original morphology, they exhibit better battery performance than the Sn particles do. Comparison of our results to other literature reports is discussed below.

Employing SnO_2 as a potential anode material for LIBs has been attempted in many studies.[21,22] Unfortunately, the oxide suffered from a high first-cycle irreversible capacity during the first charging because it has to be reduced to metallic Sn. To solve this problem, it is anticipated that metallic Sn could be applied directly. However, utilizing the metal presents another difficulty as discussed earlier. It undergoes enormous volume variation during the Li alloying and dealloying processes.[17,20] One possible solution for this is to use nanostructured hollow and/or porous Sn containing materials. It is anticipated that the local empty spaces may accommodate the large volume change.[52,53] Another possible answer is to restrain the active phases by controlling the size and morphology of the electrode materials. To achieve these, many nanostructured core–shell and composite materials have been developed.[9–11,25] Literature reports related to solving the issues are summarized in Table S1 in the ESI.† For example, the initial capacity of SnO_2 nanotubes (NTs) was 940 mA h g^{-1}. After eighty cycles at 0.05 mA cm^{-2}, a capacity of 525 mA h g^{-1} was retained, corresponding to 55.8% of the initial value.[21] In another example, SnO_2–core/C–shell NTs were investigated.[22] This nanocomposite could be repeatedly charged and discharged up to two hundred cycles with a capacity of 542 mA h g^{-1} at 0.3 mA cm^{-2}. Some Sn metal containing cases presented in Table S1† are discussed below. For hydrobenzamide-capped Sn, a charge capacity of 500 mA h g^{-1} was observed after thirty cycles at 0.2C.[23] In the second case, electrochemical tests of vertical arrays of 1D Sn NWs on Si substrates showed that a discharge capacity of 400 mA h g^{-1} could be maintained after fifteen cycles at a high discharge–charge rate of 4200 mA g^{-1}.[24] Cases of Sn@C@CNT nanostructures and rambutan-like Sn–C nanocomposites offered capacities of 490 mA h g^{-1} and 311 mA h g^{-1}, respectively.[9,10] Lastly, examples of nanocomposites of Sn and Group 11 metals are presented. Sn@Cu core–shell NPs retained a capacity of 560 mA h g^{-1} after one hundred seventy cycles at a rate of 0.8C.[25] The discharge capacity of Sn NPs supported on nanoporous Au was found to be 440 mA h g^{-1} after one hundred forty cycles at 0.1C.[11] Performance of the devices fabricated from our core–shell NWs compares favorably against the results of the better ones shown in Table S1.† The capacity of 525 mA h g^{-1} was retained after one hundred cycles at a rate of 100 mA g^{-1}. Even at a high rate of 1000 mA g^{-1} for one hundred cycles, our cell maintained a capacity of 486 mA h g^{-1}.

4. Conclusions

In summary, we have fabricated Sn@C core–shell NWs in high yields by a simple and straightforward process. By reacting vapor phase C_2H_2 with SnO_2 solids, we grew the 1D NWs *via* the VSRG pathway. Due to the unique 1D core–shell morphology, which provides an adequate void volume inside the flexible C shell, the NWs can respond to the large volume change caused by the formation and decomposition of Li_xSn alloys in the charge–discharge steps in LIBs. The electrodes show high reversible capacities, low rates of capacity fading, and consistent cycling performance. We anticipate that the core–shell NWs can be utilized for LIBs upon further optimization.

Acknowledgements

We thank the support from the National Science Council, "Aim for the Top University Plan" of the National Chiao Tung University, and the Ministry of Education of Taiwan, the Republic of China.

Notes and references

1 M. Armand and J. M. Tarascon, *Nature*, 2008, **451**, 652–657.
2 B. Kang and G. Ceder, *Nature*, 2009, **458**, 190–193.
3 M. S. Whittingham, *MRS Bull.*, 2008, **33**, 411–419.
4 P. L. Taberna, S. Mitra, P. Poizot, P. Simon and J. M. Tarascon, *Nat. Mater.*, 2006, **5**, 567–573.
5 L.-F. Cui, R. Ruffo, C. K. Chan, H. Peng and Y. Cui, *Nano Lett.*, 2008, **9**, 491–495.
6 Y. Oumellal, A. Rougier, G. A. Nazri, J. M. Tarascon and L. Aymard, *Nat. Mater.*, 2008, **7**, 916–921.
7 Y.-K. Sun, S.-T. Myung, B.-C. Park, J. Prakash, I. Belharouak and K. Amine, *Nat. Mater.*, 2009, **8**, 320–324.
8 B. L. Ellis, K. T. Lee and L. F. Nazar, *Chem. Mater.*, 2010, **22**, 691–714.
9 Y. Wang, M. Wu, Z. Jiao and J. Y. Lee, *Chem. Mater.*, 2009, **21**, 3210–3215.
10 D. Deng and J. Y. Lee, *Angew. Chem., Int. Ed.*, 2009, **48**, 1660–1663.
11 Y. Yu, L. Gu, X. Lang, C. Zhu, T. Fujita, M. Chen and J. Maier, *Adv. Mater.*, 2011, **23**, 2443–2447.
12 P. Wu, N. Du, J. Liu, H. Zhang, J. Yu and D. Yang, *Mater. Res. Bull.*, 2011, **46**, 2278–2282.
13 B.-S. Lee, S.-B. Son, K.-M. Park, J.-H. Seo, S.-H. Lee, I.-S. Choi, K.-H. Oh and W.-R. Yu, *J. Power Sources*, 2012, **206**, 267–273.
14 G. Derrien, J. Hassoun, S. Panero and B. Scrosati, *Adv. Mater.*, 2007, **19**, 2336–2340.
15 H. Nara, Y. Fukuhara, A. Takai, M. Komatsu, H. Mukaibo, Y. Yamauchi, T. Momma, K. Kuroda and T. Osaka, *Chem. Lett.*, 2008, **37**, 142–143.
16 I. A. Courtney, J. S. Tse, O. Mao, J. Hafner and J. R. Dahn, *Phys. Rev. B: Condens. Matter Mater. Phys.*, 1998, **58**, 15583–15588.
17 M. Winter and J. O. Besenhard, *Electrochim. Acta*, 1999, **45**, 31–50.
18 M. Winter, G. H. Wrodnigg, J. O. Besenhard, W. Biberacher and P. Novak, *J. Electrochem. Soc.*, 2000, **147**, 2427–2431.
19 M. Wachtler, M. Winter and J. O. Besenhard, *J. Power Sources*, 2002, **105**, 151–160.
20 B. Veeraraghavan, A. Durairajan, B. Haran, B. Popov and R. Guidotti, *J. Electrochem. Soc.*, 2002, **149**, A675–A681.
21 Y. Wang, J. Y. Lee and H. C. Zeng, *Chem. Mater.*, 2005, **17**, 3899–3903.
22 Y. Wang, H. C. Zeng and J. Y. Lee, *Adv. Mater.*, 2006, **18**, 645–649.
23 Y. Kwon, M. G. Kim, Y. Kim, Y. Lee and J. Cho, *Electrochem. Solid-State Lett.*, 2006, **9**, A34–A38.
24 J.-H. Kim, S. Khanal, M. Islam, A. Khatri and D. Choi, *Electrochem. Commun.*, 2008, **10**, 1688–1690.
25 M. G. Kim, S. Sim and J. Cho, *Adv. Mater.*, 2010, **22**, 5154–5158.
26 K. T. Lee, Y. S. Jung and S. M. Oh, *J. Am. Chem. Soc.*, 2003, **125**, 5652–5653.

27 M.-Y. Yen, C.-W. Chiu, C.-H. Hsia, F.-R. Chen, J.-J. Kai, C.-Y. Lee and H.-T. Chiu, *Adv. Mater.*, 2003, **15**, 235–237.
28 C.-H. Hsia, M.-Y. Yen, C.-C. Lin, H.-T. Chiu and C.-Y. Lee, *J. Am. Chem. Soc.*, 2003, **125**, 9940–9941.
29 C.-H. Huang, Y.-H. Chang, C.-Y. Lee and H.-T. Chiu, *Langmuir*, 2005, **22**, 10–12.
30 C.-H. Wang, H.-K. Lin, T.-Y. Ke, T.-J. Palathinkal, N.-H. Tai, I. N. Lin, C.-Y. Lee and H.-T. Chiu, *Chem. Mater.*, 2007, **19**, 3956–3962.
31 Joint Committee for Powder Diffraction (JCPDS), File No. 86-2265 and File No. 72-1147, International Center for Diffraction Data, 2002.
32 Y. Wang, D. C. Alsmeyer and R. L. McCreery, *Chem. Mater.*, 1990, **2**, 557–563.
33 J. Schwan, S. Ulrich, V. Batori, H. Ehrhardt and S. R. P. Silva, *J. Appl. Phys.*, 1996, **80**, 440–447.
34 Z. Ying, Q. Wan, Z. T. Song and S. L. Feng, *Nanotechnology*, 2004, **15**, 1682.
35 Reaction-Web, Facility for the Analysis of Chemical Thermodynamics; CRCT, http://www.crct.polymtl.ca.
36 X. M. Sun, J. F. Liu and Y. D. Li, *Chem. Mater.*, 2006, **18**, 3486–3494.
37 R. S. Wagner and W. C. Ellis, *Appl. Phys. Lett.*, 1964, **4**, 89–90.
38 I. A. Courtney, W. R. McKinnon and J. R. Dahn, *J. Electrochem. Soc.*, 1999, **146**, 59–68.
39 P. Meduri, C. Pendyala, V. Kumar, G. U. Sumanasekera and M. K. Sunkara, *Nano Lett.*, 2009, **9**, 612–616.
40 N. C. Li, C. R. Martin and B. Scrosati, *Electrochem. Solid-State Lett.*, 2000, **3**, 316–318.
41 Y. S. Jung, K. T. Lee, J. H. Ryu, D. Im and S. M. Oh, *J. Electrochem. Soc.*, 2005, **152**, A1452–A1457.
42 D. Aurbach, A. Zaban, Y. Ein-Eli, I. Weissman, O. Chusid, B. Markovsky, M. Levi, E. Levi, A. Schechter and E. Granot, *J. Power Sources*, 1997, **68**, 91–98.
43 J. L. Tirado, R. Santamaría, G. F. Ortiz, R. Menéndez, P. Lavela, J. M. Jiménez-Mateos, F. J. Gómez García, A. Concheso and R. Alcántara, *Carbon*, 2007, **45**, 1396–1409.
44 W.-M. Zhang, J.-S. Hu, Y.-G. Guo, S.-F. Zheng, L.-S. Zhong, W.-G. Song and L.-J. Wan, *Adv. Mater.*, 2008, **20**, 1160–1165.
45 M. M. Thackeray, *Handbook of Battery Materials*, Wiley-VCH, Weinheim, 1999, p. 383.
46 G.-A. Nazri and G. Pistoia, *Lithium Batteries: Science and Technology*, Kluwer Academic Plenum, Boston, 2004, p. 144.
47 R. A. Huggins, *Advanced Batteries: Materials Science Aspects*, Springer, New York, 2009, p. 131.
48 D. Aurbach, B. Markovsky, I. Weissman, E. Levi and Y. Ein-Eli, *Electrochim. Acta*, 1999, **45**, 67–86.
49 G. T. Wu, C. S. Wang, X. B. Zhang, H. S. Yang, Z. F. Qi, P. M. He and W. Z. Li, *J. Electrochem. Soc.*, 1999, **146**, 1696–1701.
50 D. Ahn, X. Xiao, Y. Li, A. K. Sachdev, H. W. Park, A. Yu and Z. Chen, *J. Power Sources*, 2012, **212**, 66–72.
51 J. W. Suk, S. Murali, J. An and R. S. Ruoff, *Carbon*, 2012, **50**, 2220–2225.
52 X. W. Lou, Y. Wang, C. Yuan, J. Y. Lee and L. A. Archer, *Adv. Mater.*, 2006, **18**, 2325–2329.
53 X. W. Lou, D. Deng, J. Y. Lee and L. A. Archer, *Chem. Mater.*, 2008, **20**, 6562–6566.